

1-1-2012

# A Coupled Experimental and Computational Approach to Quantify Deleterious Hemodynamics, Vascular Alterations, and Mechanisms of Long-Term Morbidity in Response to Aortic Coarctati

Arjun Menon

*Marquette University*, arjun.menon@marquette.edu

David C. Wendell

*Marquette University*

Hongfeng Wang

*Marquette University*, hongfeng.wang@marquette.edu

Thomas J. Eddinger

*Marquette University*, thomas.eddinger@marquette.edu

Jeffrey M. Toth

*Marquette University*, jeffrey.toth@marquette.edu

*See next page for additional authors*

---

**Authors**

Arjun Menon, David C. Wendell, Hongfeng Wang, Thomas J. Eddinger, Jeffrey M. Toth, Ronak Jashwant Dholakia, Paul M. Larsen, Eric S. Jensen, and John F. LaDisa

# A Coupled Experimental and Computational Approach to Quantify Deleterious Hemodynamics, Vascular Alterations, and Mechanisms of Long-Term Morbidity in Response to Aortic Coarctation

Arjun Menon

*Department of Biomedical Engineering, Marquette University  
Milwaukee, WI*

David C. Wendell

*Department of Biomedical Engineering, Marquette University  
Milwaukee, WI*

Hongfeng Wang

*Department of Biomedical Engineering, Marquette University  
Milwaukee, WI*

Thomas J. Eddinger

*Department of Biological Sciences, Marquette University  
Milwaukee, WI*

**Jeffrey M. Toth**

*Department of Biomedical Engineering, Marquette University  
Department of Orthopaedic Surgery, Medical College of  
Wisconsin  
Milwaukee, WI*

**Ronak J. Dholakia**

*Cerebrovascular Center, Stony Brook University Medical Center  
Stony Brook, NY*

**Paul M. Larsen**

*Tulane University School of Medicine  
New Orleans, LA*

**Eric S. Jensen**

*Biomedical Resource Center, Medical College of Wisconsin  
Department of Pediatrics, Children's Hospital and the Medical  
College of Wisconsin  
Milwaukee, WI*

**John F. LaDisa**

*Department of Biomedical Engineering, Marquette University  
Department of Pediatrics, Children's Hospital and the Medical  
College of Wisconsin  
Milwaukee, WI*

## **Abstract**

### *Introduction*

Coarctation of the aorta (CoA) is associated with morbidity despite treatment. Although mechanisms remain elusive, abnormal hemodynamics and vascular biomechanics are implicated. We present a novel approach that facilitates quantification of coarctation-induced mechanical alterations and their impact on vascular structure and function, without genetic or confounding factors.

## *Methods*

Rabbits underwent thoracic CoA at 10 weeks of age (~9 human years) to induce a 20 mmHg blood pressure (BP) gradient using permanent or dissolvable suture thereby replicating untreated and corrected CoA. Computational fluid dynamics (CFD) was performed using imaging and BP data at 32 weeks to quantify velocity, strain and wall shear stress (WSS) for comparison to vascular structure and function as revealed by histology and myograph results.

## *Results*

Systolic and mean BP was elevated in CoA compared to corrected and control rabbits leading to vascular thickening, disorganization and endothelial dysfunction proximally and distally. Corrected rabbits had less severe medial thickening, endothelial dysfunction, and stiffening limited to the proximal region despite 12 weeks of normal BP (~4 human years) after the suture dissolved. WSS was elevated distally for CoA rabbits, but reduced for corrected rabbits.

## *Discussion*

These findings are consistent with alterations in humans. We are now poised to investigate mechanical contributions to mechanisms of morbidity in CoA using these methods.

**Keywords:** fluid dynamics, shear stress, vascular remodeling

## **Introduction**

Coarctation of the aorta (CoA) is the most common congenital heart defect, occurring in 8–11% of births annually [1, 2]. Surgical techniques have evolved over the last half century, and postoperative outcomes have improved dramatically as a result. Unfortunately life expectancy for patients with CoA remains reduced despite these advancements due to long-term morbidity in the form of hypertension, early-onset coronary artery disease, and aneurysm formation. It has been postulated that these sources of morbidity can be explained on the basis of abnormal hemodynamics and vascular biomechanics in the thoracic aorta and its branches [3], but the specific factors and mechanisms responsible remain elusive.

Investigation into the hemodynamic and biomechanical basis of morbidity in CoA is intriguing considering recent advancements in computational modeling. Anatomic data obtained from a routine imaging session, in concert with physiological data such as phase-contrast MRI (PC-MRI) and blood pressure (BP), can be used to create 3D subject-specific representations of hemodynamics that consider vascular properties associated with the current patient state. Although this approach is now being applied for patients with CoA [4], the direct link between altered indices and changes in the vasculature is difficult to establish due to the limited number and heterogeneity of patients at any given center.

The objective of this work was to develop an in vivo model that can be used to quantify alterations in hemodynamic and vascular biomechanics indices including BP, flow, velocity, indices of wall shear stress (WSS) and strain caused by CoA, as well as the impact of these alterations on vascular morphology and function. Specifically we aimed to reproduce changes in these indices observed in untreated (i.e. native) CoA distinctly from those occurring after the common surgical treatment of resection with end-to-end anastomosis. We begin with a description of the methods and protocol developed for this purpose, followed by examples of their application with image-based computational fluid dynamics (CFD) and experimental techniques including histology and myograph vascular analysis to test the hypothesis that abnormal hemodynamics are related to coarctation-induced structural and functional changes in the aorta and its branches.

## **2. Methods**

### ***2.1. Experimental protocol***

All experimental procedures were approved by the Animal Care and Use Committee of Marquette University and the Medical College of Wisconsin. Furthermore, all conformed to the "Guiding Principles in the Care and Use of Animals" of the American Physiological Society and the *Guide for the Care and Use of Laboratory Animals* as outlined by the National Research Council. After no less than 72 hours of acclimation, male New Zealand white rabbits ~10 weeks old and

weighing 0.8–1.2 kg were randomly designated to undergo descending thoracic CoA using silk (permanent) or Vicryl (dissolvable) suture to mimic untreated and treated CoA patient populations, respectively. A control group was also established. Rabbits undergoing CoA were anesthetized with ketamine and xylazine (22 and 2.5 mg/kg IM, respectively), underwent endotracheal intubation, and were then maintained on a ventilator throughout the procedure with 1–2% isoflurane. Cefazolin (20 mg/kg SQ) was administered at least 1 hour prior to the first incision. Fur above the 3–8th intercostal spaces was shaved and prepped for sterile surgery using an antiseptic solution. CoA was then induced through a left thoracotomy in the third intercostal space. Muscular and tissue layers were carefully and gently navigated to expose to the proximal descending thoracic aorta (dAo). 3-0 silk (CoA group) or Vicryl (corrected group) ligatures were then tied around the aorta against a 16 gauge (1.6 mm) diameter stainless steel wire. Removal of the wire resulted in a coarctation of repeatable and known size causing a 15–20 mmHg BP gradient across the coarctation at harvest as verified with early rabbits. Importantly, the putative guideline suggestive of treatment for CoA in humans is a BP gradient  $\geq 20$  mmHg at rest [5].

To evacuate the pneumothorax caused by coarctation induction, a flexible chest tube was inserted into the pleural cavity through a small incision made near the 8th rib. The tube was passed subcutaneously rostral two intercostal spaces and positioned within the pleural cavity. The externalized end of the tube was secured by a purse-string suture. The chest was then closed in layers and suction was applied to the chest tube using a syringe and 3-way stopcock. The chest tube was removed  $\sim 1.5$  hours after surgery when the rabbit was sternal and no additional air or fluid could be evacuated.

## *2.2 Surgical monitoring, post-operative care and pharmacologic regimen*

Exceptional procedural and postoperative monitoring was necessary for success. Extensive monitoring was conducted during all experimental procedures using quantitative criteria with preferred operating ranges for oxygen saturation, heart and respiratory rate, temperature, mucous membrane color and capillary refill time.



Monitoring was conducted at ten-minute intervals during procedures, as well as for 4–5 hours after surgery and 2–3 hours after the MRI procedures discussed below. Buprenorphine (0.025 mg/kg SQ) and cefazolin (20 mg/kg SQ) were administered for postoperative analgesia and antibiotic prophylaxis, respectively, for two days after surgery. Qualitative criteria such as attitude, appetite, urination, defecation, vomiting and appearance of the surgical site were recorded along with the quantitative criteria above 2, 3, 5, 10 and 14 days after surgery and periodically thereafter. Furosemide was also administered for two weeks post-op (4 mg/kg SQ BID) and as needed thereafter to treat any ensuing respiratory symptoms due to pulmonary edema. Rabbits were provided with enrichment in 4×8 ft runs.

### *2.3 Anatomic and phase contrast magnetic resonance imaging (MRI)*

Rabbits underwent anatomic and phase contrast MRI for use with CFD modeling and for determination of cyclic vascular strain upon reaching adult size (32–36 weeks of age). Anesthesia was administered as described above and a saline-filled angiocath IV was inserted into the left marginal ear vein for contrast-enhanced illumination of the thoracic aorta and its branches. Cardiovascular MRI was conducted with a 3T GE Sigma Excite scanner (GE Healthcare, Waukesha, WI) using a quadrature knee coil and the sequences shown in Table 1. To ensure adequate anesthesia, pulse oximeter (Nonin Medical Inc, Plymouth, MN) and core temperature sensors approved for use in the MR environment were included. Two doses (0.2 mmol/kg, ~0.4 ml/kg) of gadolinium (Gd; Omniscan gadodiamide; GE Healthcare, Princeton, NJ) were prepared and loaded into the distal end of extension tubing that was connected to the angiocath IV. Additional saline-filled extension tubing was also attached to the IV and an MR-compatible pump within the scanner room. Gd-enhanced MR angiography (MRA) was performed at an injection rate of 2 ml/sec.

	<b>MRA</b>	<b>PC-MRI</b>
Sequence	3D fast GRE	2D fastcard PC
TR/TE/flip angle	6.0 ms/1.7 ms/30 degrees	8.5 ms/1.7 ms/20 degrees
slice thickness	1.2 mm	3.0 mm
acquisition matrix (pixels)	256 × 192	256–384 × 224–256
field of view (cm)	12 × 12	12 × 12
VENC (cm/sec)	-	80–200
cardiac frames	-	20

**Table 1** Magnetic Resonance Imaging Parameters

Blood flow information for use with CFD was acquired using a cardiac-gated, 2D, PC-MRI sequence with through-plane velocity encoding. PC images were obtained at planes transverse to the ascending aorta (AscAo), the cervical arteries, the coarctation, and dAo.

## 2.4 CFD simulations

Computational representations of the aorta and the arteries of the head and neck were created for each group as described previously [4]. Briefly, AscAo PC-MRI waveforms were mapped to the inlet face of CFD models using a temporally varying parabolic flow profile. Flow waveforms obtained from the head and neck arteries were used with measured BP data to prescribe outflow boundary conditions. To replicate the physiologic effect of arterial networks distal to CFD model branches, three-element Windkessel model [6] outlet boundary conditions were imposed using a coupled-multidomain method [7, 8]. This method provides an intuitive representation of the arterial tree beyond model outlets and can be described by three parameters with physiologic meaning: characteristic (i.e. regional) resistance ( $R_c$ ), arterial capacitance ( $C$ ) and distal resistance ( $R_d$ ). The total arterial capacitance (TAC) for control and corrected rabbits was determined from inflow and BP measurements assuming a characteristic-to-total resistance ratio of 6% [9] and adjusted for the CoA group according to previous literature [10]. The TAC was then distributed among outlets according to their flow distributions [11]. Once the capacitance terms for each branch were assigned, the terminal resistance ( $R_t$ ) was calculated from mean BP and flow measurements and distributed between the  $R_c$  and  $R_d$  parameters by

adjusting Rc:Rt ratios to replicate measured BP using the pulse pressure method [12, 13].

Simulations were then performed using a novel stabilized finite element method to solve equations for the conservation of mass (continuity) and balance of fluid momentum (Navier-Stokes). Vessels were modeled as rigid and blood was assumed to be a Newtonian fluid with a density of 1.06 g/cm<sup>3</sup> and a viscosity of 4 cP consistent with a previous report in rabbits [14] and upon consideration of shear rates observed in the current investigation. Computational meshes contained ~4 million tetrahedral elements and localized refinement was performed using an adaptive technique to deposit more elements in regions prone to flow disruption [15]. Simulations were run for 4–6 cardiac cycles until the flow rate and BP fields yielded periodic solutions.

Results for blood flow velocity, BP and WSS were visualized using ParaView (Kitware, Inc., Clifton Park, NY). Time-averaged WSS (TAWSS) and oscillatory shear index (OSI) were then calculated [16]. Low TAWSS is thought to promote atherogenesis, as is elevated OSI, an index of directional changes in WSS. Low OSI indicates WSS is unidirectional, while a value of 0.5 is indicative of bidirectional WSS with a time-average value of zero. Previous imaging studies found local low TAWSS and elevated OSI values that were statistically different from circumferential averages [17], motivating the need to report detailed local WSS results in CFD studies. Therefore, circumferential values were extracted at several locations in the dAo. Circumferential results at each location were divided into 16 sectors of equal size and values within each sector were averaged.

## *2.5 Measurement of blood pressure and tissue harvest*

After detailed offline analysis of MRI data, rabbits were again anesthetized for measurement of BP prior to tissue harvest. Proximal and distal BP waveforms are measured simultaneously and obtained with the same model transducer (Harvard Apparatus, Holliston, MA) from which waveforms were digitally recorded at 720 Hz using a computer interfaced with an analog-to-digital converter. Transducers were attached to 5 inch noncompliant fluid-filled catheters. The proximal fluid-filled catheter was inserted into the common carotid

artery and tracked retrogradely to the aortic arch. The distal fluid-filled catheter was inserted into the femoral artery and tracked retrogradely to the aortoiliac bifurcation. Rabbits were euthanized after BP measurement by an intravenous overdose of pentobarbital sodium (100 mg/kg). The dAo above (proximal) and below (distal) the coarctation were excised with care to avoid damaging the endothelium or vascular smooth muscle tissue and regions of interest were fixed with 4% Paraformaldehyde for histology, or placed in ice-cold physiological salt solution (PSS) in preparation for myographic analysis.

## *2.6 Histological analysis*

After a fixation period of >24 hours, portions of arteries from the regions mentioned above underwent a controlled 49-hour infiltration protocol involving progressive dehydration with graded ethanols, clearing in xylene, followed by paraffin infiltration. Arteries were then oriented and embedded in paraffin wax, sectioned at a thickness of 5 microns, floated on warm water bath, mounted on clear glass slides and dried. Spatial landmarks were made on sections so morphometric measurements could be correlated to circumferential CFD data. Verhoeff Van Gieson staining was used to identify internal elastic lamina (IEL), media, elastic fibers, and the external elastic lamina (EEL). Tissues were carefully stained so that elastin could be differentiated. Slight color differences between samples were alleviated by white balancing and exposure time adjustment during image capture. Stained sections were then cover slipped and digital micrographs were acquired with a digital camera coupled to a light microscope using consistent 6.3x and 16x objective lenses. Subsequent analysis was performed using ImageJ after calibration for magnification strength. Quantification was performed for total medial thickness (distance between the IEL and EEL) and medial portions of sections that were disorganized as evident by fragmentation and elastin coloration differences within the region from the IEL progressing radially. All quantifications were conducted in triplicate by three investigators blinded to the experimental group.

## 2.7 Myograph analysis

Vascular ring specimens 3–4 mm in length were carefully sectioned from the dAo locations mentioned above and cleaned of adhering perivascular tissue. Each ring was placed in a 10ml, water-jacketed and temperature controlled (37°C) organ bath and mounted on two stainless steel hooks: one fixed to the bottom of the bath and the other connected to a high-fidelity Grass force transducer for accurate measurement of tension. The bath was filled with PSS and continuously bubbled with oxygen. Aortic rings were stretched under 1–2 grams of tension and allowed to equilibrate for at least 1 hour. In a preliminary set of experiments, length-tension contractions with a high potassium PSS solution (KPSS) were conducted to determine the appropriate resting tension at which testing should be conducted to accurately reflect resting tension in the physiological state (10–20% of total KPSS active tension [18]). In agreement with previous studies [19], initial tests found that KPSS contractions with a resting tension of 2 g consistently resulted in the desired range of total force. All experiments were therefore conducted at this value and continuously recorded on pre-calibrated channels.

After the equilibration period, KPSS contractions were conducted at resting tension followed by a 3x PSS rinse. This procedure was repeated 2–3 times to ensure a consistent effective force response from arteries. After a second equilibration period of at least 1 hour, a subsequent experiment was conducted to observe endothelium-dependent relaxation via nitric oxide (NO) release. Briefly, arteries were pre-contracted with 0.2  $\mu\text{M}$  PE. Once tension values stabilized, cumulative addition of the endothelium-dependent muscarinic receptor agonist acetylcholine (ACh;  $10^{-9}$  to  $10^{-5}$  M) was initiated, and relaxation response curves were quantified as a percentage of pre-contracted active tension. Acetylcholine has been used extensively to observe the endothelium's capacity to synthesize NO and thus vasodilate in response to blood flow.

## 2.8 Statistical analysis

All data shown is expressed as mean  $\pm$  standard error of the mean (SEM). Statistical evaluations were performed using one-way

ANOVA, followed by Tukey post-hoc analysis. A  $P$ -value  $<0.05$  was considered statistically significant.

### **3. Results**

#### ***3.1 Experimental protocol***

Twenty-eight animals have been included in the protocol described and representative results are provided here for three rabbits in each group for which all desired indices have been quantified to date. There were no differences in weight between rabbits in each experimental group at the conclusion of the experimental protocol (control=3.1 vs Native=3.0 and Corrected=3.2 kg). Five animals underwent humane euthanasia prior to completion of the study. One rabbit weighing 1.8 kg at CoA induction developed congestive heart failure. As a result, the strict arrival weight criterion of 1.2 kg described was implemented to limit the likelihood of this occurrence. Necropsies from two additional animals indicated pasteurella pneumonia as revealed generalized by a mottled appearance and firmness to the lungs that affected all lobes. A third rabbit was found to have a dilated thin-walled right ventricle thought to be congenital as well as anomalous mesenteric torsion 48 hours after the procedure. A fifth rabbit developed respiratory issues secondary to problems incurred during intubation.

#### ***3.2 Anatomic and phase contrast MRI***

Maximum intensity projections of the MRA data from one representative rabbit of each group are shown in Figure 1. Rabbits undergoing CoA with silk suture developed pronounced stenosis following surgery, thereby resembling the human condition of untreated CoA. In contrast, rabbits undergoing CoA with dissolvable suture developed a similar stenosis initially as verified by MRI. However, degradation of the suture 56–70 days (average=63 days) after surgery restored aortic diameter close to normal, but with modest residual narrowing within the coarctation region, thus mimicking vascular morphology commonly observed following the human surgical treatment of resection with end-to-end anastomosis. Control rabbits represented healthy subjects of similar age and weight.

Rabbits undergoing coarctation developed tortuosity distal to the stenosis that was more severe for CoA than corrected rabbits. Cardiac output from phase contrast MRI data taken near the sinuses in the AscAo was used to determine inflow waveforms for CFD as shown in the lower portion of Figure 1. Although differences did not reach significance, cardiac output was most elevated in rabbits mimicking untreated CoA ( $445 \pm 48$  ml/min), and to a lesser extent for rabbits in the group mimicking treated CoA ( $404 \pm 27$  ml/min) when compared to control ( $371 \pm 40$  ml/min). AscAo mean diameter delineated from PC-MRI magnitude images was larger for both CoA ( $8.0 \pm 0.4$  mm) and corrected ( $8.1 \pm 0.4$  mm) as compared to control ( $7.1 \pm 0.2$  mm) rabbits, but this difference also did not reach significance. Cyclic strain was significantly elevated for CoA as compared to corrected and control rabbits. Moreover, the elastic pressure strain modulus ( $E_p$ ), an index of vascular stiffness calculated from PC-MRI and the BP measurements discussed below as  $E_p = [(BP_s - BP_d)/(D_s - D_d)]/D_{\text{mean}}$  where D is the AscAo diameter during systole(s) and diastole(d), was significantly different ( $P < 0.05$ ) between groups (eg. CoA =  $41.3 \pm 10.2 \times 10^4$  N/m<sup>2</sup> vs. corrected =  $14.1 \pm 1.7 \times 10^4$  N/m<sup>2</sup> vs. control =  $0.84 \pm 0.22 \times 10^4$  N/m<sup>2</sup>).

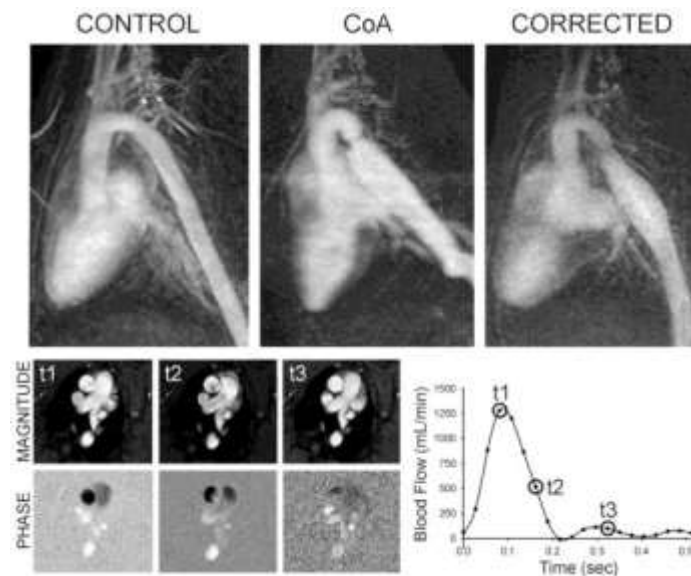


**Figure 1**

Maximum intensity projections of MRA data from one representative rabbit in each experimental group (top). Phase-contrast MRI data was used in the CFD process. Magnitude data (lower left) measured in the ascending aorta was



additionally used to calculate diameter, cyclic strain, and in conjunction with phase data to generate inflow waveforms for CFD (lower right).

### 3.3 Blood pressure measurements

Representative ensemble-averaged waveforms from rabbits in each group are shown in Figure 2. Implementation of the coarctation resulted in a significant increase in systolic and mean BP, as well as an increased mean BP gradient of  $20 \pm 3$  mmHg ( $P < 0.05$ ) across the coarctation region as compared to control ( $4 \pm 3$  mmHg; Fig 3). Implementation of the dissolvable suture resulted in systolic and mean BP, as well as a mean BP gradient ( $5 \pm 3$  mmHg), that were statistically similar to control and significantly different from CoA rabbits ( $P < 0.05$ ).

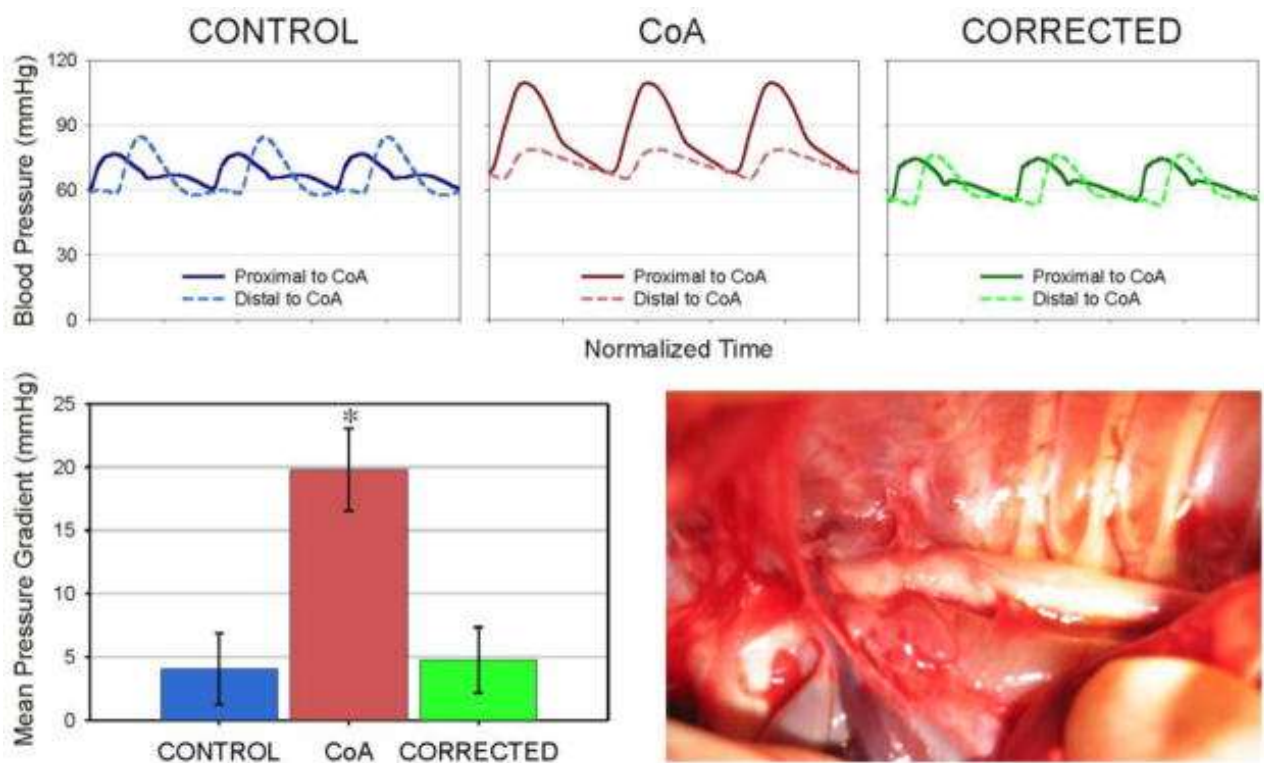


**Figure 2**

Representative ensemble-averaged waveforms from rabbits (top) are shown along with the mean blood pressure gradients in each experimental group (left) and an image of the thoracic aorta with coarctation just prior to tissue harvest (right). \* = significantly different ( $P < 0.05$ ) from control.



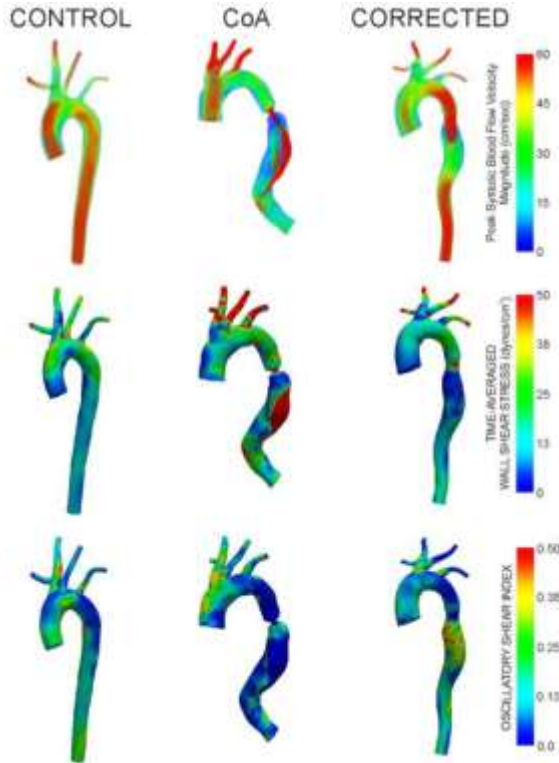


**Figure 3**

Peak systolic blood flow velocity, time-averaged wall shear stress, and oscillatory shear index from representative rabbits in each experimental group.

### 3.4 CFD simulation results

Peak systolic blood flow velocity, TAWSS, and OSI are displayed for representative rabbits from each group in Figure 3. Peak systolic velocity profiles in control rabbits are generally parabolic with values  $>60$  cm/s throughout the aorta and its branches. While similar findings are observed for CoA rabbits, a region of post-stenotic dilation just distal to the coarctation was consistently observed. The coarctation also introduces a velocity jet that impinges on the downstream posterior wall for these rabbits. Corrected rabbits had lower peak systolic velocity values in the AscAo, likely due to larger dimensions in this region. Interestingly, these rabbits had elevated velocity within the coarctation region due to residual narrowing.

TAWSS distributions within the dAo of the three groups were consistent with the velocity patterns mentioned above. Control rabbits

revealed fairly uniform distributions of TAWSS with a spatial average of  $\sim 15$  dyn/cm<sup>2</sup>. In contrast, CoA rabbits had pronounced regions of low TAWSS proximal and distal to the coarctation with extremely high TAWSS within the coarctation and along the downstream dAo wall where the velocity jet impinged. Corrected rabbits also showed regions of low TAWSS proximal and immediately distal to the coarctation region. Their TAWSS values within the slightly narrowed coarctation region were less pronounced and TAWSS values in the downstream dAo more closely resembled those seen in control rabbits, but with a rotating patterns due to vessel tortuosity. Flow separation as quantified by OSI revealed values of  $\sim 0.25$  in the dAo of control rabbits. CoA rabbits experienced low OSI proximal and downstream of the coarctation, with elevated values immediately distal to the stenosis. Corrected rabbits showed similar trends above the coarctation, but with pronounced OSI distal to residual narrowing in this region.

### *3.5 Local distributions of TAWSS*

Circumferential TAWSS values were extracted from converged CFD simulations results for regions in the proximal and distal dAo near where histological and myograph artery sections were obtained (Fig 4). Spatially equivalent regions were queried for all rabbits using the worst-case CoA rabbits as a guide. Thus, the proximal region represents the approximate midway location between the left subclavian artery and coarctation, while the distal region represents the center of the impact zone created by the impinging velocity jet. There were no significant differences between experimental groups at any circumferential sectors proximal to the coarctation. Spatial patterns showed highest TAWSS values along the outer (posterior) luminal surface, and lowest values along the inner (anterior) surface. The outer left luminal surface of the distal dAo was exposed to pronounced and significantly ( $P < 0.05$ ) elevated TAWSS in CoA as compared to control and corrected rabbits. In contrast, TAWSS was significantly reduced at several sectors along the right luminal surface in corrected as compared to control and CoA rabbits.

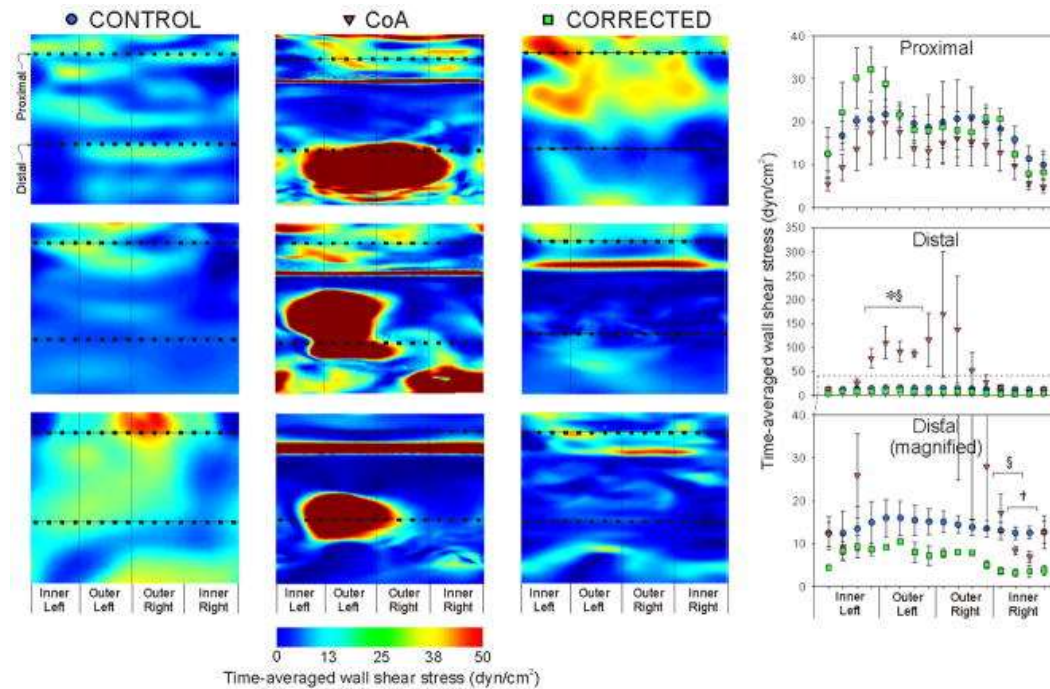


**Figure 4**

Circumferential TAWSS extracted from converged CFD simulations results for regions in the proximal and distal descending thoracic aorta near where histological and myograph artery sections were obtained. Spatially equivalent regions were queried for all rabbits using CoA rabbits as a guide. The proximal region represents the approximate midway location between the origin of the left subclavian artery and coarctation, while the distal region represents center of the impact zone created by the impinging velocity jet. The right bottom graph is a magnified version of the distal location to more clearly show differences between control and corrected circumferential values. \* = CoA significantly different ( $P<0.05$ ) from control; † = corrected significantly different ( $P<0.05$ ) from control; § = CoA significantly different ( $P<0.05$ ) from corrected.

### 3.6 Histological Analysis

Verhoeff Van Gieson stained arterial sections representative of the proximal and distal dAo for each experimental group are shown in Figure 5 (left images). Total medial thickness proximal to the coarctation was significantly increased ( $P<0.05$ ) for rabbits in both the CoA and corrected groups as compared to spatially equivalent locations from controls (Fig 5, right plots). Hashed portions of the plots indicate the amount of the media containing disorganized lamellae that

was not present in the control group. There were no differences in total medial thickness between groups distal to coarctation, but disorganized lamellae were again present in CoA and corrected rabbits. Interestingly, the thickness of the organized portion of the medial layer was similar for all groups proximal to the CoA. This was also true distal to the coarctation.



**Figure 5**

Verhoeff Van Gieson stained arterial sections representative of sections obtained proximal and distal to the coarctation region in CoA and corrected groups as compared to spatially equivalent locations from control rabbits. Hashed portions of the plots indicate the amount of the medial layer containing fragmented lamellae devoid of darkly-stained elastin. Upward error bars correspond to the SEM for the entire medial thickness while downward error bars represent the SEM for hashed portions of the plots. \* = significantly different (P<0.05) from control.

### 3.7 Acetylcholine relaxation analysis

Active vasorelaxation curves in response to ACh for rings extracted proximal and distal to the coarctation are shown in Figure 6. Proximal to the coarctation, the aorta of control rabbits is able to relax nearly 80% of pre-contracted tension. In contrast, CoA and corrected rabbits showed significantly ( $P<0.05$ ) diminished relaxation at all concentrations greater than  $[1E-7]$  when compared to control, with a maximal relaxation of only 33% in corrected and 6% in CoA rabbits. CoA aortas also showed significant difference from those of corrected rabbits at the highest ACh concentration.

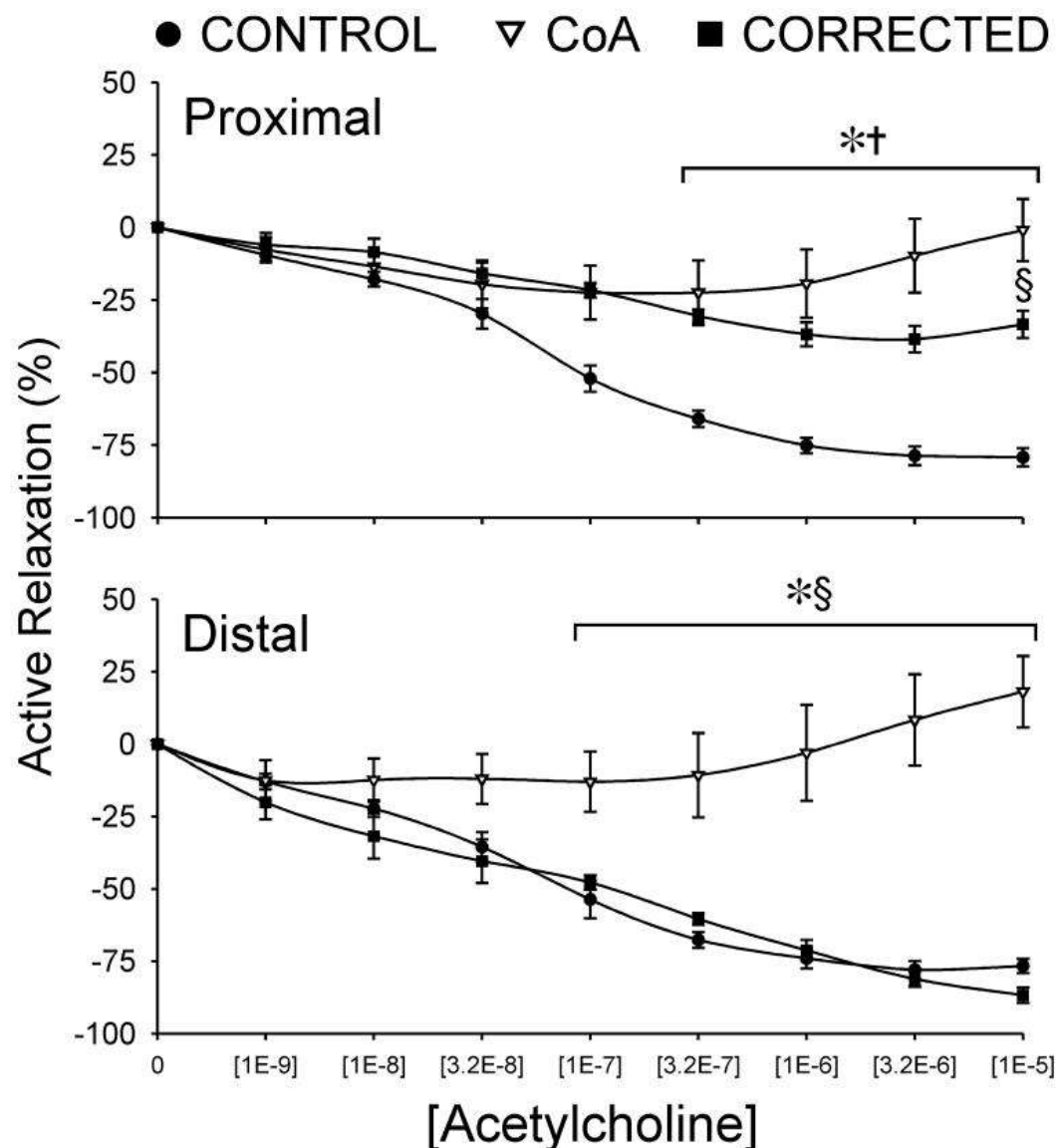


**Figure 6**

Active vasorelaxation curves in response to ACh for rings of aortic tissue extracted proximal and distal to the coarctation region in CoA and corrected groups as compared to spatially equivalent locations from control rabbits. \* = CoA significantly different ( $P < 0.05$ ) from control; † = corrected significantly different ( $P < 0.05$ ) from control; § = CoA significantly different ( $P < 0.05$ ) from corrected.

No significant differences were observed in the ACh-derived vasorelaxation between the control and corrected groups distal to the coarctation with active relaxation reaching 77% and 81%, respectively, at the maximum concentration administered. However,



CoA relaxation at ACh doses greater than  $[3.2\text{E-}7]$  was impaired ( $P<0.01$ ) with peak relaxation of only 13%.

## 4. Discussion

Despite a common perception of CoA as a simple disease, the natural history to date includes a reduced lifespan as compared to the normal population. While neonatal CoA may result in life threatening situations early postnatally with the closing of the ductus arteriosus, these can now be resolved with low mortality through a number of surgical approaches. Unfortunately, many patients still appear destined to develop long-term morbidity, the most notable of which is hypertension during rest and/or exercise, as well as early onset coronary artery disease and the potential for aneurysm formation. Thus, it may be that CoA is a syndrome of etiological problems rather than simply a single anatomical constriction of the aorta. Alternatively, the CoA may lead to a series of consequences throughout the body that are only moderately reversible following surgical correction of the coarctation. Reduced arterial compliance and decreased baroreceptor reflex sensitivity [20, 21], impaired vascular function [22, 23], and over activity of the renin-angiotensin system [24], have all been implicated in the paradoxical hypertension occurring in patients with surgically corrected CoA. Our inability to identify the mechanism(s) associated with in CoA such as essential hypertension precludes any expectation that an adequate treatment or cure can truly be identified for these individuals. This issue is confounded by the limited number and heterogeneity of patients at any given center.

In order to address this situation, we have developed an animal model coupled with experimental and computational techniques that allows us to uniquely quantify mechanical alterations induced by untreated as well as treated CoA and their impact on structure and function in the cardiovascular system, all independent of any genetic predisposition and/or confounding factors. As compared to other animal models of coarctation that implement excessive BP gradients often placed in the abdominal aorta [25, 26], our model leads to a BP gradient in the thoracic aorta that mimics the putative guideline for treatment of CoA in humans, and facilitates longitudinal study to determine long-term consequences of the disease. Moreover, the

current rabbit coarctation model provides a unique multiscale approach to investigate possible residual morbidities present after surgical repair. Initial results with this model reveal several changes in local hemodynamics and vascular structure and function previously reported in CoA patients. These findings are summarized below.

### *Morphology, blood pressure and image-based quantification*

The current experimental model mimics alterations in local vascular geometry seen in native and treated CoA patients. Mean intensity projections created from MRA data of CoA rabbits are similar to those of many native CoA patients without collateral vessels. The caliber of intercostal arteries at harvest suggests collaterals may be present, but just not resolved by 3T imaging. Rabbits in which the coarctation was induced by dissolvable suture consistently revealed modest wasting in the coarctation region, a finding commonly observed after surgical resection with end-to-end anastomosis. BP measurements taken above and below the coarctation at harvest verify that a 20 mmHg BP gradient develops, consistent with the putative treatment guideline in humans, and results in elevated mean and systolic BP that persists in CoA rabbits for the duration of the study. While a pop test has not been performed with BP measurement equipment to date, use of the same transducers and stock from which fluid-filled catheters were created suggests that the time shift denoted by the foot of BP waveforms (Fig 2) is physiologic. The trends towards increased proximal diameter, decreased strain indicative of elevated stiffness in CoA, and elevated cardiac output reflective of a persistent hyperdynamic state even after repair are also consistent with reported findings in humans [27–29].

### *Indices of wall shear stress*

In a recent study of healthy young adults [17] areas of low TAWSS and elevated OSI were found in a rotating pattern progressing down the dAo. A study of ten middle-aged adults with pre-existing plaques revealed similar WSS patterns that correlated with areas of atherosclerotic plaque [30]. Unfortunately there are very few studies reporting patterns of WSS in coarctation to date. CFD was used in the

current investigation to obtain detailed spatiotemporal quantification of hemodynamics based on MRI and BP data. The general patterns of TAWSS and OSI reported here correspond well with the available data [4]. The local quantification presented in this pilot work suggests TAWSS is important distal to the coarctation where the high velocity jet and associated TAWSS may play a role in the tortuosity observed [31] as well as changes in vascular function discussed below.

## *Vascular structure and function*

It was postulated nearly 50 years ago that the aorta adapts to maintain a preferential vascular wall stress (generally expressed as the product of BP and radius) by thickening through the addition of medial lamellar units [32]. This earlier work indicates that under normal conditions vascular wall composition and behavior are similar across multiple species including rabbits. However, the current work focuses on the thoracic aorta of rabbits in response to elevated BP that, in some cases, is then alleviated. While the preliminary data presented here suggested there are still changes in thickness responsible for maintaining preferential wall stress, the current results also suggest this index may be maintained not purely by medial lamellar units, but also by disorganized vascular tissue that helps to provide stiffness proximal to the coarctation.

To date, the model described here has revealed persistent deleterious alterations in vascular structure and endothelial dysfunction 12 weeks following coarctation repair, and in the absence of resting hypertension. Importantly, structural alterations and endothelial dysfunction have also been reported in humans with CoA [33, 34]. The findings from the current model are intriguing and may be of cellular and/or acellular origins. Future work will further examine individual structural components in the vessel wall and characterize vascular behavior in response to additional agents to determine participation of specific receptors, channels and second messenger pathways in the findings demonstrated here.

The current methods are also amenable to the study of interventional treatments for CoA. For example, Figure 7 shows results obtained from a rabbit after stent implantation. Although stenting for CoA was first conducted in 1991 [35], many questions persist



pertaining to the use of this technology including the impact of making ~30% of the dAo nearly rigid, changes in afterload following implantation and how blood flow disruptions downstream of the stent may influence indices of WSS previously shown to correlate with the location and severity of plaque deposition [17, 30]. The current model can likely lend insight to many of these questions.

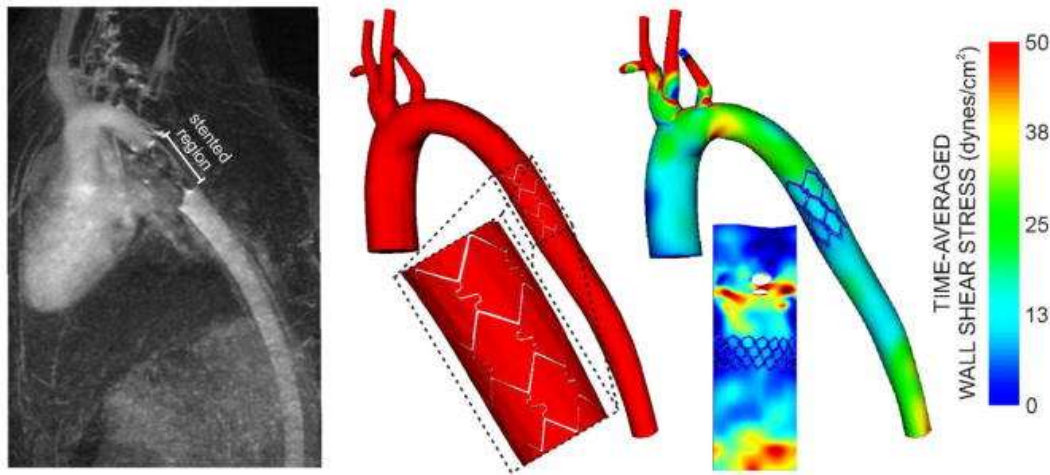


**Figure 7**

Example showing how the methods described can also be used to quantify changes in hemodynamics and vascular biomechanics in response to stent implantation. The mean intensity projection of MRA data is shown (left) along with a CFD model containing the implanted stent (middle) and time-averaged wall shear stress results (right). These results have also been unwrapped about the interior curvature of the aorta for clarity.

The current results should be interpreted within the constraints of several potential limitations. The goal of this work was to describe a coupled experimental and computational approach to uniquely investigate sources of morbidity using a clinically representative animal model of CoA. Thus, representative results from a sampling of rabbits are presented here and must be confirmed in a larger investigation. Nonetheless, the complexity and importance of details inherent to these methods make them worthy of dissemination. Surgery was conducted when rabbits were ~10 weeks of age (~9 years old in humans) [36, 37]. Patients with CoA generally present shortly after birth or during adolescence. The current model may therefore be more amenable to the latter group of patients whose vasculature has a chance to gradually adapt as they grow in to the

coarctation. The suture used with corrected rabbits is designed to dissolve by 63 days after surgery suggesting that the coarctation was alleviated at least three months, an equivalent of 4 human years [36, 37], before the completion of the experiment. It is unclear whether the observed alterations would persist in corrected rabbits at a later time point, and future studies will address this question. Numerous studies have indicated long-term outcomes are more favorable when surgical correction is implemented earlier in life ( $< 1$  year) [22]. The current results suggest the severity of the coarctation and the duration it is present may be more important than the absolute age of correction since our rabbits were not newborns at the onset of CoA.

The ability of our CFD outlet boundary conditions to match aimed systolic and diastolic BP values in the proximal thoracic aorta has been shown previously [38]. However, little data is available on the agreement of measured and simulation BP values in the dAo and matching of waveform contours at either location. Figure 8 shows that while systolic values are similar between measured and simulated BP, there are several important differences resulting from limitations in the methods applied for the current investigation. Measured BP waveforms from control and corrected rabbits show a phase lag and increase in pulse BP between proximal and distal waveforms. The phase lag is due to capacitance within the vessel wall that was not included in the rigid CFD model simulations conducted here. Importantly, it has been shown that 60% of the total arterial capacitance is located in the proximal thoracic aorta [13] and decreases distally leading to spatially-varying tissue properties that account for increased rigidity, wave reflection and pulse BP amplification relative to upstream locations [39]. The methods used in the current investigation also do not account for this heterogeneity in tissue properties and therefore result in similar simulation waveform contours proximally and distally. In contrast, BP waveforms from CFD simulations of CoA rabbits are similar to those measured in vivo likely because the proximal reflecting point has been moved closer to the heart with the introduction of the coarctation. The coarctation also dampens the BP pulse manifesting in the distal thoracic aorta as shown for both the measured and simulated waveforms, but the lack of spatially-varying tissue properties causes the distal pulse BP in the CFD simulation to be lower than that measured in vivo. Recent advances in CFD modeling are now beginning to account for aortic capacitance [40] and spatially-varying

tissue properties (personal communication - C.A. Figueroa). Future CFD studies using the experimental model introduced here will attempt to incorporate similar methods to facilitate further agreement between proximal and distal BP waveforms obtained through CFD simulations and in vivo measurement.

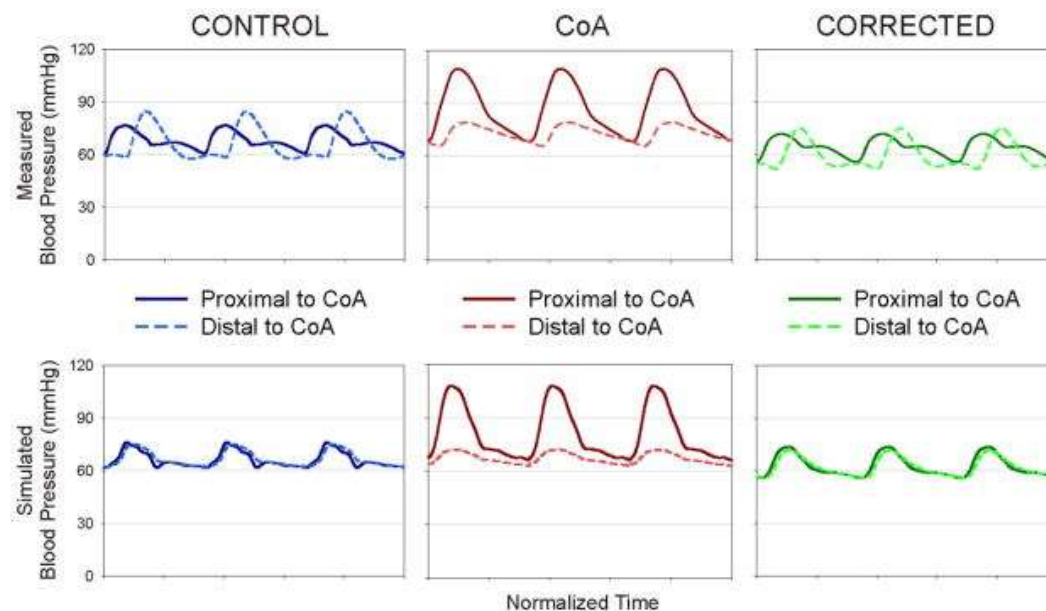


**Figure 8**

Comparison of proximal and distal BP waveform contours measured in vivo to those obtained from CFD simulations. While systolic and diastolic values are similar between measured and simulated BP, the use of rigid walls and the lack of spatially varying tissue properties during CFD modeling accounts for the observed differences mentioned in the limitations portion of the discussion.

## Conclusion

In summary, we report the details of a novel coupled experimental and computational approach that facilitates quantification of mechanical alterations induced by untreated as well as treated CoA and their impact on structure and function in the cardiovascular system, all independent of any genetic predisposition and/or confounding factors. The present methodology is highly reproducible and has generated preliminary results consistent with CoA findings in humans. Under the controlled conditions afforded by these methods, we are now uniquely poised to investigate mechanisms associated with

residual morbidity in patients with CoA as well as the effectiveness of current and next-generation treatment approaches.

## Acknowledgments

The authors gratefully acknowledge Tina Kostenko, Yu Liu, Eric Paulson and Julie Peay (Dept. of Biophysics, Medical College of Wisconsin) for imaging assistance, Christy Stadig and Wale Sulaiman (Dept. of Neuroscience/Neuroscience Research Labs, Medical College of Wisconsin) for the use of monitoring equipment during imaging sessions, and John Tessmer and David Schwabe (Dept. of Anesthesiology, Medical College of Wisconsin) for experimental assistance.

**Sources of funding:** This work was supported by an AREA award from the National Institutes of Health (R15HL096096-01 to JFL) and assistance from the Alvin and Marion Birnschein Foundation (to JFL).

## Footnotes

**Publisher's Disclaimer:** This is a PDF file of an unedited manuscript that has been accepted for publication. As a service to our customers we are providing this early version of the manuscript. The manuscript will undergo copyediting, typesetting, and review of the resulting proof before it is published in its final citable form. Please note that during the production process errors may be discovered which could affect the content, and all legal disclaimers that apply to the journal pertain.

## References

1. Ferencz C, Rubin JD, McCarter RJ, Brenner JI, Neill CA, Perry LW, Hepner SI, Downing JW. Congenital heart disease: Prevalence at livebirth. The baltimore-washington infant study. *American Journal of Epidemiology*. 1985;12:31–36.
2. Roger VL, Go AS, Lloyd-Jones DM, Adams RJ, Berry JD, Brown TM, Carnethon MR, Dai S, de Simone G, Ford ES, Fox CS, Fullerton HJ, Gillespie C, Greenlund KJ, Hailpern SM, Heit JA, Ho PM, Howard VJ, Kissela BM, Kittner SJ, Lackland DT, Lichtman JH, Lisabeth LD, Makuc DM, Marcus GM, Marelli A, Matchar DB, McDermott MM, Meigs JB, Moy CS, Mozaffarian D, Mussolino ME, Nichol G, Paynter NP, Rosamond WD, Sorlie PD, Stafford RS, Turan TN, Turner MB, Wong ND, Wylie-Rosett J. Heart disease and stroke statistics--2011 update: A report from the american heart association. *Circulation*. 2011;123:e18–e209.

3. O'Rourke MF, Cartmill TB. Influence of aortic coarctation on pulsatile hemodynamics in the proximal aorta. *Circulation*. 1971;44:281–292.
4. LaDisa JF, Jr, Dholakia RJ, Figueroa CA, Vignon-Clementel IE, Chan FP, Samyn MM, Cava JR, Taylor CA, Feinstein JA. Computational simulations demonstrate altered wall shear stress in aortic coarctation patients previously treated by resection with end-to-end anastomosis. *Congenital Heart Disease*. 2011.
5. Rosenthal E. Stent implantation for aortic coarctation: The treatment of choice in adults? *J Am Coll of Cardiol*. 2001;38:1524–1527.
6. Westerhof N, Stergiopulos N, Noble MIM. *Snapshots of hemodynamics an aid for clinical research and graduate education*. New York: Springer; 2005.
7. Vignon-Clementel IE, Figueroa CA, Jansen KE, Taylor CA. Outflow boundary conditions for 3d simulations of non-periodic blood flow and pressure fields in deformable arteries. *Comput Methods Biomech Biomed Engin*. 2010;13:625–640.
8. Vignon-Clementel IE, Figueroa CA, Jansen KE, Taylor CA. Outflow boundary conditions for three-dimensional finite element modeling of blood flow and pressure in arteries. *Comput Methods Appl Mech Eng*. 2006;195:3776–3796.
9. Laskey WK, Parker HG, Ferrari VA, Kussmaul WG, Noordergraaf A. Estimation of total systemic arterial compliance in humans. *J Appl Physiol*. 1990;69:112–119.
10. Stergiopulos N, Westerhof N. Determinants of pulse pressure. *Hypertension*. 1998;32:556–559.
11. Stergiopulos N, Young DF, Rogge TR. Computer simulation of arterial flow with applications to arterial and aortic stenoses. *J Biomech*. 1992;25:1477–1488.
12. O'Rourke MF, Safar ME. Relationship between aortic stiffening and microvascular disease in brain and kidney: Cause and logic of therapy. *Hypertension*. 2005;46:200–204.
13. Stergiopulos N, Segers P, Westerhof N. Use of pulse pressure method for estimating total arterial compliance in vivo. *Am J Physiol Heart Circ Physiol*. 1999;276:H424–428.
14. Windberger U, Bartholovitsch A, Plasenzotti R, Korak KJ, Heinze G. Whole blood viscosity, plasma viscosity and erythrocyte aggregation in nine mammalian species: Reference values and comparison of data. *Exp Physiol*. 2003;88:431–440.
15. Muller J, Sahni O, Li X, Jansen KE, Shephard MS, Taylor CA. Anisotropic adaptive finite element method for modelling blood flow. *Comput Methods Biomech Biomed Engin*. 2005;8:295–305.
16. Les AS, Shadden SC, Figueroa CA, Park JM, Tedesco MM, Herfkens RJ, Dalman RL, Taylor CA. Quantification of hemodynamics in abdominal

- aortic aneurysms during rest and exercise using magnetic resonance imaging and computational fluid dynamics. *Ann Biomed Eng.* 2010;38:1288–1313.
17. Frydrychowicz A, Stalder AF, Russe MF, Bock J, Bauer S, Harloff A, Berger A, Langer M, Hennig J, Markl M. Three-dimensional analysis of segmental wall shear stress in the aorta by flow-sensitive four-dimensional-mri. *J Magn Reson Imaging.* 2009;30:77–84.
  18. Speich JE, Almasri AM, Bhatia H, Klausner AP, Ratz PH. Adaptation of the length-active tension relationship in rabbit detrusor. *Am J Physiol Renal Physiol.* 2009;297:F1119–1128.
  19. Gauthier KM, Chawengsub Y, Goldman DH, Conrow RE, Anjaiah S, Falck JR, Campbell WB. 11(r),12(s),15(s)-trihydroxyeicosa-5(z),8(z),13(e)-trienoic acid: An endothelium-derived 15-lipoxygenase metabolite that relaxes rabbit aorta. *Am J Physiol Heart Circ Physiol.* 2008;294:H1467–1472.
  20. Polson JW, McCallion N, Waki H, Thorne G, Tooley MA, Paton JF, Wolf AR. Evidence for cardiovascular autonomic dysfunction in neonates with coarctation of the aorta. *Circulation.* 2006;113:2844–2850.
  21. Vogt M, Kuhn A, Baumgartner D, Baumgartner C, Busch R, Kostolny M, Hess J. Impaired elastic properties of the ascending aorta in newborns before and early after successful coarctation repair: Proof of a systemic vascular disease of the prestenotic arteries? *Circulation.* 2005;111:3269–3273.
  22. de Divitiis M, Pilla C, Kattenhorn M, Zadinello M, Donald A, Leeson P, Wallace S, Redington A, Deanfield JE. Vascular dysfunction after repair of coarctation of the aorta: Impact of early surgery. *Circulation.* 2001;104:I165–170.
  23. Brili S, Tousoulis D, Antoniadis C, Aggeli C, Roubelakis A, Papathanasiu S, Stefanadis C. Evidence of vascular dysfunction in young patients with successfully repaired coarctation of aorta. *Atherosclerosis.* 2005;182:97–103.
  24. Parker FB, Jr, Streeten DH, Farrell B, Blackman MS, Sondheimer HM, Anderson GH., Jr Preoperative and postoperative renin levels in coarctation of the aorta. *Circulation.* 1982;66:513–514.
  25. Lee SK, Kim HS, Song YJ, Joo HK, Lee JY, Lee KH, Cho EJ, Cho CH, Park JB, Jeon BH. Alteration of p66shc is associated with endothelial dysfunction in the abdominal aortic coarctation of rats. *FEBS Lett.* 2008;582:2561–2566.
  26. Vaziri ND, Ni Z. Expression of nox-i, gp91(phox), p47(phox) and p67(phox) in the aorta segments above and below coarctation. *Bba-Gen Subjects.* 2005;1723:321–327.



27. Morrison TM, Choi G, Zarins CK, Taylor CA. Circumferential and longitudinal cyclic strain of the human thoracic aorta: Age-related changes. *J Vasc Surg.* 2009;49:1029–1036.
28. Nielsen JC, Powell AJ, Gauvreau K, Marcus EN, Prakash A, Geva T. Magnetic resonance imaging predictors of coarctation severity. *Circulation.* 2005;111:622–628.
29. Pacileo G, Pisacane C, Russo MG, Crepaz R, Sarubbi B, Tagliamonte E, Calabro R. Left ventricular remodeling and mechanics after successful repair of aortic coarctation. *Am J Cardiol.* 2001;87:748–752.
30. Wentzel JJ, Corti R, Fayad ZA, Wisdom P, Macaluso F, Winkelman MO, Fuster V, Badimon JJ. Does shear stress modulate both plaque progression and regression in the thoracic aorta? Human study using serial magnetic resonance imaging. *J Am Coll Cardiol.* 2005;45:846–854.
31. Sho E, Nanjo H, Sho M, Kobayashi M, Komatsu M, Kawamura K, Xu C, Zarins CK, Masuda H. Arterial enlargement, tortuosity, and intimal thickening in response to sequential exposure to high and low wall shear stress. *J Vasc Surg.* 2004;39:601–612.
32. Wolinsky H, Glagov S. A lamellar unit of aortic medial structure and function in mammals. *Circ Res.* 1967;20:99–111.
33. Gardiner HM, Celermajer DS, Sorensen KE, Georgakopoulos D, Robinson J, Thomas O, Deanfield JE. Arterial reactivity is significantly impaired in normotensive young adults after successful repair of aortic coarctation in childhood. *Circulation.* 1994;89:1745–1750.
34. Vriend JW, de Groot E, de Waal TT, Zijta FM, Kastelein JJ, Mulder BJ. Increased carotid and femoral intima-media thickness in patients after repair of aortic coarctation: Influence of early repair. *Am Heart J.* 2006;151:242–247.
35. O’Laughlin MP, Perry SB, Lock JE, Mullins CE. Use of endovascular stents in congenital heart disease. *Circulation.* 1991;83:1923–1939.
36. Masoud I, Shapiro F, Kent R, Moses A. A longitudinal study of the growth of the new zealand white rabbit: Cumulative and biweekly incremental growth rates for body length, body weight, femoral length, and tibial length. *J Orthop Res.* 1986;4:221–231.
37. Three Little Ladies Rabbitry. Rabbit / human years table. 2011 <http://www.threelittleladiesrabbitry.com/rabbityears.php>.
38. LaDisa JF, Jr, Figueroa CA, Vignon-Clementel IE, Kim HJ, Xiao N, Ellwein LM, Chan FP, Feinstein JA, Taylor CA. Computational simulations for aortic coarctation: Representative results from a sampling of patients. *J Biomech Eng.* 2011.
39. Nichols WW, O’Rourke MF. McDonald’s blood flow in arteries: Theoretical, experimental and clinical principles. 5. New York: Hodder Arnold; 2005.

40. Figueroa CA, Vignon-Clementel IE, Jansen KE, Hughes TJR, Taylor CA. A coupled momentum method for modeling blood flow in three-dimensional deformable arteries. *Comput Methods Appl Mech Eng.* 2006;195:5685–5706.